processes

MDPI

Article

Dye Photocatalytic Degradation and Water Treatment Using Biosynthetic ZnO Nanoparticles Produced Using Annatto Tree Leaf Extract

Aparecido de J. Bernardo [1,†], Andrei N. G. Dabul [2,†], Moudo Thiam [1,†], Vanessa O. A. Pellegrini [1], Mariana A. Silva [2], Sreedevi Vallabhapurapu [3], Sachin Desarada [3], Vijaya Srinivasu Vallabhapurapu [4], Carla R. Fontana [2] and Igor Polikarpov [1,*]

[1] Institute of Physics, University of São Paulo, Avenida Joao Dagnone, 1100, Jardim Santa Angelina, São Carlos 13563-120, SP, Brazil; ajbernardo@usp.br (A.d.J.B.); moudothiam_.167@usp.br (M.T.); varnoldi@yahoo.com.br (V.O.A.P.)
[2] School of Pharmaceutical Sciences, São Paulo State University, Rodovia Araraquara-Jaú, km 01, Araraquara 14800-903, SP, Brazil; nicoli.dabul@unesp.br (A.N.G.D.); mariana.almeida-silva@unesp.br (M.A.S.); carla.fontana@unesp.br (C.R.F.)
[3] School of Computing, University of South Africa, 28 Pioneer Avenue, Florida Park, Johannesburg 1710, South Africa; vallas@unisa.ac.za (S.V.); sdesarada@gmail.com (S.D.)
[4] Physics Department, University of South Africa, 28 Pioneer Avenue, Florida Park, Johannesburg 1710, South Africa; vallavs@unisa.ac.za
* Correspondence: ipolikarpov@ifsc.usp.br
† These authors contributed equally to this work.

Abstract

The biosynthesis of zinc oxide nanoparticles (ZnO NPs) using plant extracts offers several important advantages, including low residue generation, reduced costs, and potentially faster production as compared to traditional chemical methods. In this study, for the first time, ZnO NPs were biosynthesized using an annatto plant (*Bixa orellana*) leaf extract and characterized using a range of analytical techniques, including scanning electron microscopy, X-ray diffraction, energy-dispersive X-ray spectroscopy, ultraviolet–visible and Fourier transform infrared spectroscopies, thermogravimetric analysis, and point of zero charge measurements, thus ensuring a comprehensive elucidation of their physicochemical properties. Subsequently, photodegradation of methylene blue (MB) dye using the biosynthesized ZnO NPs was successfully demonstrated. The photodegradation studies showed that the ZnO NPs were capable of decomposing over 95% of MB after 110 min of UV irradiation. In addition, the potential application of ZnO NPs for water disinfection was evaluated by assessing their ability to eliminate microbial pathogens. Furthermore, cell-free singlet oxygen and intracellular ROS detection assays were performed to investigate the NP antibacterial molecular mechanisms. Overall, our results reveal that the ZnO NPs exhibit excellent potential for photodegradation applications and may contribute to the development of more effective and sustainable solutions for water treatment and quality control.

Keywords: ZnO nanoparticles; biosynthesis; ROS; photocatalytic degradation; bacterial disinfection; water control

Academic Editor: Andrea Petrella

Received: 14 December 2025
Revised: 11 January 2026
Accepted: 26 January 2026
Published: 28 January 2026

1. Introduction

Recent scientific advances have enabled the development of green synthesis of zinc oxide nanoparticles (ZnO NPs) using plant-derived extracts. In contrast to traditional phys-

ical and/or chemical synthesis methods, green-synthesized nanoparticles offer advantages such as reduced residue generation during the synthesis process and lower toxicity, which are beneficial to the environment [1]. In this approach, plant extracts act as stabilizing agents during nanoparticle formation, thereby enhancing bioavailability and environmental compatibility compared with conventionally synthesized nanoparticles [2].

Annatto tree (*Bixa orellana*) is a tropical plant native to the Americas and is well-known for its reddish seeds, which are rich in carotenoids and used as food pigments [3]. Chemical compounds present in annatto seeds, including terpenes, steroids, and carotenoids, exhibit considerable therapeutic properties, with the reported photoprotective, antioxidant, antidiabetic, anti-inflammatory, antimicrobial, anticancer, and anthelmintic characteristics [3]. Owing to their unique physicochemical properties, ZnO NPs have been extensively investigated as photocatalytists. ZnO exhibits high stability, low toxicity, and strong UV-driven photocatalytic activity. Furthermore, due to their simple implementation and high efficiency, ZnO NPs have also been widely applied in wastewater treatment [4].

Water is an essential natural resource for all living organisms. Moreover, modern life relies heavily on water in numerous industrial applications, ranging from food production and pharmaceutical manufacturing to a wide array of other industries. Due to the recurrent mismanagement of sewage, industrial, and agricultural wastes, various bacterial species are often found in water sources, with the *Enterobacteriaceae* family microorganisms, such as *Escherichia coli* and *Salmonella* spp., frequently being prevalent. Additionally, structural factors like aging pipelines and branched network systems promote the formation of bacterial biofilms, including those formed by the waterborne pathogen *Pseudomonas aeruginosa* [5–7]. The presence of antibiotic-resistant bacteria and antibiotic resistance genes in aquatic environments, particularly in wastewater, poses a significant global health concern, as these elements can disseminate through various routes, contributing to the spread of antimicrobial resistance to humans and animals [8].

Given the enormous scale of water distribution networks, selecting practical and effective methods for bacterial decontamination is essential. However, although decontamination is crucial for eliminating pathogens in water used for various purposes, such as drinking and recreational activities, this process might present significant challenges, particularly when potential selection of resistant strains is considered [9]. The residues of decontamination agents that remain in the environment, even at subinhibitory levels, can pose a significant threat since the mutations conferring resistance typically incur a low fitness cost [10]. Another important consideration is that, unlike mutations induced by high-dose exposures, which tend to be highly specific, those selected by low doses often accumulate over time. These mutations can interfere with a broad range of chemical agents, potentially complicating future decontamination efforts [10].

Considering all these factors, the use of metal oxide nanoparticles for water disinfection may offer significant advantages, primarily due to the non-specific nature of their antibacterial mechanisms [11]. Unlike traditional methods that target specific receptors or biomolecules, metal oxide nanoparticles reduce the likelihood of bacterial resistance build-up due to their multifactorial mode of action [12].

Here, we explore the use of annatto plant leaf extracts for the biosynthesis of ZnO NPs. The resulting NPs were characterized using a range of analytical techniques, and their photocatalytic activity in dye degradation was evaluated. In addition, the antibacterial properties of NPs were investigated, with a particular focus on common waterborne pathogenic microorganisms, and compared with those of ZnO NPs previously synthesized using coffee leaf extracts [13] and other ZnO NPs. Moreover, their potential molecular antibacterial mechanisms were assessed using cell-free singlet oxygen and intracellular ROS detection assays.

2. Experimental/Methods

2.1. Materials

Fresh annatto plant (*Bixa orellana*) leaves were collected at a local rural farm in Itápolis, Sao Paulo State, Brazil. Sodium hydroxide (NaOH), zinc nitrate hexahydrate ($Zn(NO_3)_2 \cdot 6H_2O$), and all organic solvents were purchased from Sigma-Aldrich (Burlington, MS, USA). Ultrapure water was used in all experiments.

2.2. Preparation of Annatto Plant Leaf Extracts

The leaves were thoroughly rinsed with ultrapure water to eliminate dust particles and oven-dried at 35 °C for one week. After drying, the leaves were ground using a knife mill and stored in plastic bags at room temperature. To obtain water-soluble extractives, 20 g (dry weight) of the ground material was suspended in 150 mL of ultrapure water and autoclaved at 120 °C for 30 min. Finally, the aqueous extract was filtered to remove residual solids.

2.3. Synthesis of Zinc Oxide Nanoparticles Using Annatto Plant Leaf Extracts

Zinc nitrate hexahydrate was added to the annatto plant leaf extract as a precursor at a mass-to-volume ratio of 6:100 (w/v). The pH of the solution was adjusted to 6.5 using a 6.5 M sodium hydroxide solution, and the resulting mixture was autoclaved at 121 °C for 1 h. After autoclaving, the mixture was allowed to cool down to room temperature and then centrifuged at 13,000 rpm for 15 min at 25 °C. The supernatant was discarded, and the solid residue was washed twice with water to remove impurities. The recovered solid fraction was oven-dried at 105 °C for 24 h and subsequently calcined in a muffle furnace at 500 °C for 4 h.

2.4. Physical Characterization of NPs

2.4.1. X-Ray Diffraction Analyses

XRD analyses were performed on a Miniflex 600 X-ray diffractometer (Rigaku, Tokyo, Japan) operated at 40 kV and 15 mA. The measurements were carried out at room temperature using Cu Kα radiation (λ = 1.5406 Å). Diffraction patterns were recorded over a 2θ range of 5–70°, with an angular step of 0.02° and a counting time of 15 s per step. The diffraction peaks were extracted from experimental diffractograms using a peak-fitting software (PeakFit; Version 16, https://grafiti.com/). The average crystallite size was estimated using the modified Scherrer equation [14]. In addition, the average crystallite size (D), dislocation density (δ), and microstrain (ε) were also determined using the Williamson–Hall method [15] according to the expressions $\delta = \frac{1}{D^2}$ and $\varepsilon = \frac{\beta}{4\ tan\theta}$.

Rietveld Analysis

XRD data of the ZnO nanoparticle sample were further analyzed by the Rietveld method using the BGMN refinement engine operated through the Profex graphical user interface [16]. The refinement included background and peak-position related corrections, together with phase scale factors and unit-cell parameters, while instrumental profile contributions were treated as fixed and only sample-related peak-broadening parameters were refined. To capture the observed line-broadening behavior, a bimodal profile-broadening approach was applied, representing the diffraction profiles as the superposition of a narrow and a broad component interpreted as two crystallite-size populations and/or broadening states, which is recommended when the specimen exhibits bimodal distributions of broadening effects that are not adequately represented by a single peak-shape function. The quality of fit was evaluated using standard Rietveld agreement indicators (e.g., R_{wp} and

goodness-of-fit), and refined microstructural outputs from the bimodal model characteristic sizes of the two components and their relative contributions were evaluated.

2.4.2. UV-Vis Spectrophotometric Measurements

The optical properties of the ZnO NPs were characterized using a UV-Vis spectrophotometer (UV-2600i, Shimadzu, Nakagyō-ku, Kyoto, Japan) in a wavelength range of 220–850 nm. From the obtained optical absorption spectrum, the nanoparticle band gap was estimated using the Tauc plot method, using the following relation:

$$(\alpha h\nu)^{1/2} = A(h\nu - E_g)$$

where α is an absorption coefficient, A is a constant, $h\nu$ is the photon energy, and E_g is the band gap energy.

2.4.3. SEM and EDS Analyses

The morphological characteristics of the biosynthesized ZnO NPs were examined by scanning electron microscopy (SEM) using a field-emission scanning electron microscope (FESEM SUPRA™35, Carl Zeiss, Oberkochen, Germany) operated at an accelerating voltage of 5 kV. The samples were prepared as a 1 mg/mL suspension in ethanol and allowed to dry on the sample holder prior to analysis.

The elemental composition of the synthesized NPs was evaluated by energy-dispersive X-ray spectroscopy coupled to scanning electron microscopy (SEM-EDS) (Zeiss, LEO 440, Oberkochen, Germany). The ZnO NP powder was deposited onto carbon tape and sputter-coated with a thin layer of gold before analysis.

2.4.4. FT-IR Analysis

Infrared (IR) spectra of the samples were recorded using a Nicolet 6700 FT-IR spectrometer (Thermo Fisher Scientific, Waltham, MA, USA). The sample pellets were prepared using a hydraulic press, and the spectra were recorded in the wavenumber range of 400–4000 cm^{-1}.

2.4.5. TGA of the ZnO NPs

The thermal stability of the ZnO NPs was evaluated using a Mettler Toledo thermogravimetric analyzer (TGA Q50 V20.13; Columbus, OH, USA). Approximately 5.5 mg of the nanoparticle powder was heated up to 1000 °C at a rate of 20 °C/min under a flow of synthetic air.

2.4.6. Point of Zero Charge pH (pH_{pzc})

The point of zero charge (PZC) of the biosynthesized ZnO NPs was determined using the pH drift method. Briefly, 25 mg of ZnO NPs were added to 10 mL of NaCl solution ($C = 12.5 \times 10^{-3}$ molar) with initial pH values of 2, 4, 6, 8, 10, and 12 adjusted using NaOH, and the suspensions were stirred for 24 h. The final pH of each sample was then measured. The pH_{pzc} was determined from the plot of final pH versus initial pH as the point where the addition of the NPs does not change the pH (e.g., the final pH equals the initial pH).

2.5. Photocatalytic Activity Experiments

The biosynthesized ZnO NPs were used as a photocatalyst for methylene blue (MB) dye. In a standard photocatalysis experiment, 25 mg of the photocatalyst was dispersed in 100 mL of MB water solution with a dye concentration of 5 mg/L, with initial pH of MB. To achieve adsorption-desorption equilibrium, the mixture was stirred in the dark for 30 min. After the dark period, a mixture containing MB and the photocatalyst was irradiated with UV-A light for seven hours using eight 6-watt UV-A T-5-BL Lucmat lamps (Sao Paulo, SP,

Brazil) and a maximum emission wavelength of 368 nanometers (nm). During the course of the experiment, 1.5 mL aliquots were taken every one hour to evaluate dye degradation.

Next, to evaluate the pH dependence of MB dye photodegradation, pH of the solution was adjusted using NaOH to several different pHs (8, 10, and 12), and the photocatalytic experiments were repeated in the presence of ZnO NPs and in their absence (negative control experiments). The supernatant was subjected to centrifugation at 13,300 rpm for 10 min. The degradation of the dye was monitored by measuring the decrease in the maximum absorbance of the supernatant, with a peak centered at λ = 663 nm, using a Thermo Scientific Multiskan GO UV/Vis Microplate Reader Spectrophotometer (Thermo Scientific, Waltham, MA, USA) over a wavelength range of 200–1000 nm.

The percentage of degradation was quantified using the following equation:

$$Degradation\ percentage = \frac{C_0 - C_t}{C_0} \times 100\% = \frac{A_0 - A_t}{A_0} \times 100\%$$

Here, A_0 is the initial absorbance of dyes corresponding to the initial concentration C_0, and A_t is the absorbance with concentration C_t at time interval t.

Finally, dominant reactive oxygen species (ROS) were evaluated using the following quenchers: ethylenediaminetetraacetic acid (EDTA), dimethyl sulfoxide (DMSO), para-benzoquinone (BQ), and Isopropyl alcohol (IPA), which are scavengers of different ROS. EDTA targets photogenerated holes (h^+), DMSO scavenges electrons (e^-), BQ sequesters superoxide radicals ($O_2\bullet^-$), and IPA scavenges hydroxyl radicals ($\bullet$OH).

2.6. Determination of the Minimal Inhibitory Concentration

An NP stock suspension was prepared at a concentration of 50 mg/mL in Mueller-Hinton broth (MHB), followed by a two-fold serial dilution down to a final concentration of 1.56 mg/mL. Using a 96-well microplate, each well was filled with 160 µL of MHB, 20 µL of NP suspension, and 20 µL of bacterial suspensions of either *E. coli*, *P. aeruginosa*, or *S. enterica* at 5×10^6 CFU/mL, prepared from an overnight culture grown at 37 °C. The wells containing 200 µL of MHB alone were used as sterility controls, while those containing 180 µL of MHB and 20 µL of bacterial suspension served as growth controls. All conditions were tested in triplicate.

Due to the inherent turbidity caused by the nanoparticles in the culture medium, the conventional method of determining the Minimal Inhibitory Concentration (MIC) based on the absence of turbidity is not feasible in this case. Therefore, we employed the resazurin viability assay, which relies on the reduction in non-fluorescent resazurin to fluorescent resorufin by metabolically active cells, thus allowing for an accurate assessment of cell viability [17].

The microplate was incubated at 37 °C for 24 h, after which 40 µL of a 0.15 mg/mL resazurin solution was added to each well. Following an additional 2 h incubation at 37 °C, 100 µL from each well was transferred to a black microtiter plate for fluorescence measurement (excitation: 550 nm; emission: 590 nm). The MIC was defined as the smallest concentration of NP reducing fluorescence to the same levels as in sterility controls.

2.7. Cell-Free Singlet Oxygen Detection

To assess singlet oxygen ($^1O_2$) production in a cell-free environment, the contents of one vial (100 µg) of the fluorescent sensor Singlet Oxygen Sensor Green (Invitrogen, Carlsbad, CA, USA) were dissolved in 33 µL of methanol to prepare a 5 mM stock solution. Each nanoparticle sample was suspended in 1 mL of deionized water, and 2 µL of the stock solution was added to each suspension. As a negative control, 2 µL of the stock solution was added to 1 mL of deionized water without nanoparticles, resulting in a final sensor concentration of 10 µM in all conditions.

Aliquots of 100 µL from each experimental condition were transferred, in triplicate, to the wells of a black 96-well microtiter plate. Fluorescence was then measured with an excitation wavelength of 505 nm and 525 nm emission wavelength detection to quantify singlet oxygen generation.

2.8. Intracellular ROS Detection

Intracellular ROS production was evaluated using CM-H_2DCFDA (Invitrogen, Carlsbad, CA, USA), a general oxidative stress fluorescent probe. The contents of one vial (50 µg) were dissolved in 17 µL of dimethyl sulfoxide (DMSO) to prepare a 5 mM stock solution.

E. coli ATCC 25922, *P. aeruginosa* ATCC 27853, and *S. enterica* serovar Typhimurium ATCC 14028 were grown overnight at 37 °C. The bacterial cells were harvested by centrifugation, washed with sterile saline, and resuspended to a standardized concentration of 10^6 CFU/mL. To 1 mL of each bacterial suspension, 2 µL of the CM-H_2DCFDA stock solution was added, yielding a final probe concentration of 10 µM. The suspensions were incubated at 37 °C for 30 min, followed by centrifugation and an additional wash with sterile saline.

For the assay, 50 µL of each labeled bacterial suspension was transferred to wells of a black 96-well microtiter plate, followed by 50 µL of 5 mg/mL ZnO NPs biosynthesized using annatto leaf extracts, or sterile saline (negative control), and ZnO NPs synthesized using coffee leaf extract for comparison. All conditions were tested in triplicate. The plate was incubated for 2 h at 37 °C, after which fluorescence was measured using an excitation wavelength of 495 nm, and emission was detected at the wavelength of 520 nm.

3. Results and Discussion

3.1. Analytical Characterization of the NPs

3.1.1. X-Ray Diffraction

X-ray diffraction (XRD) was employed to evaluate the biogenic ZnO NPs synthesized using annatto plant leaf extract. Well-defined, strong diffraction peaks were observed at 2θ angles of 31.65°, 34.22°, 36.11°, 47.43°, 56.50°, 62.77°, 67.87°, and 68.98° (Figure 1a). The latter peaks are consistent with a hexagonal wurtzite structure (JCPDS 5-0664) of ZnO NPs and correspond to the crystallographic planes (100), (002), (101), (102), (110), (103), and (112), respectively. No additional secondary phases were detected in the experimental XRD patterns (Figure 1). Among the various ZnO crystalline structures, the hexagonal wurtzite form is the most stable, which is potentially advantageous for ZnO NP applications [18].

The average crystallite size was estimated using the Scherer equation [19], yielding a value of 11.8 ± 0.9 nm. The Williamson–Hall method [15] renders a similar estimate for the average crystallite size of approximately 9.88 nm (Figure 1a). Furthermore, the microcrystalline strain (ε) and dislocation density (δ) were determined as 1.5×10^{-3} and 10.2×10^{-3} nm^{-2}, respectively.

To obtain more in-depth structural analysis, the X-ray data were subjected to Rietveld refinement. The Rietveld refinement further corroborated the fact that the biogenic NPs crystallize as single-phase hexagonal wurtzite ZnO, consistent with the absence of extra reflections in the experimental pattern. Figure 2 shows the refined XRD structure, and the inset shows the crystalline structure of wurtzite ZnO. The refined lattice parameters for the two bimodal ZnO components were essentially identical in a = 0.325 nm and very close in c = 0.520–0.521 nm, which agrees well with typical room-temperature wurtzite ZnO lattice constants reported in the literature [20,21]. The bimodal microstructure model resolved two coherent-domain crystallite size populations, with ZnO1 (47 wt%) showing a larger crystallite size of 47 nm and ZnO2 (53 wt%) a smaller crystallite size of 26 nm,

indicating a broadened two-population crystallite-size distribution rather than a single average size. When weighted by the refined phase fractions, the bimodal model gives an overall fraction-weighted mean crystallite size of ~35.9 nm, highlighting that the Rietveld-derived coherent-domain size is dominated by the smaller-size contribution but still reflects the presence of a substantially larger-size fraction.

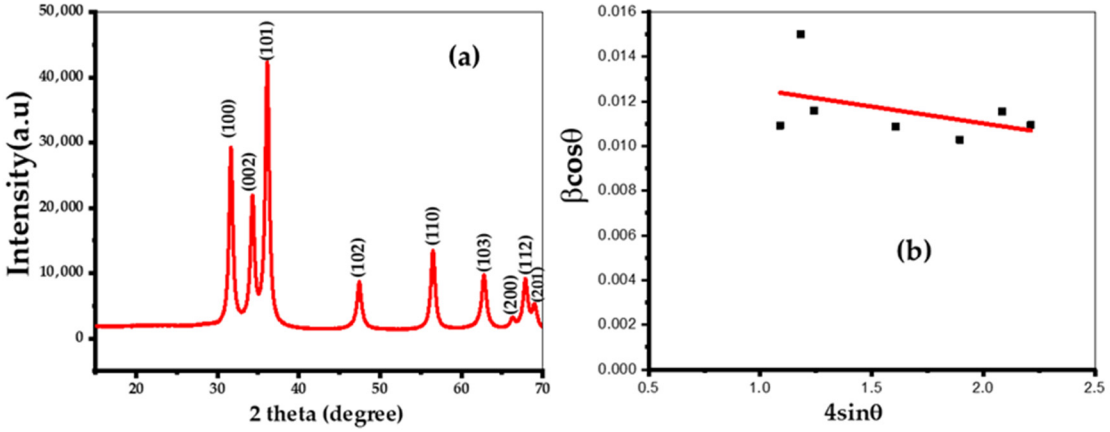

Figure 1. (**a**) X-ray diffraction (XRD) pattern of biogenic ZnO NPs synthesized using annatto tree leaf extract. (**b**) Williamson–Hall plot used for the estimation of an average crystallite size, dislocation density, and a microstrain [15].

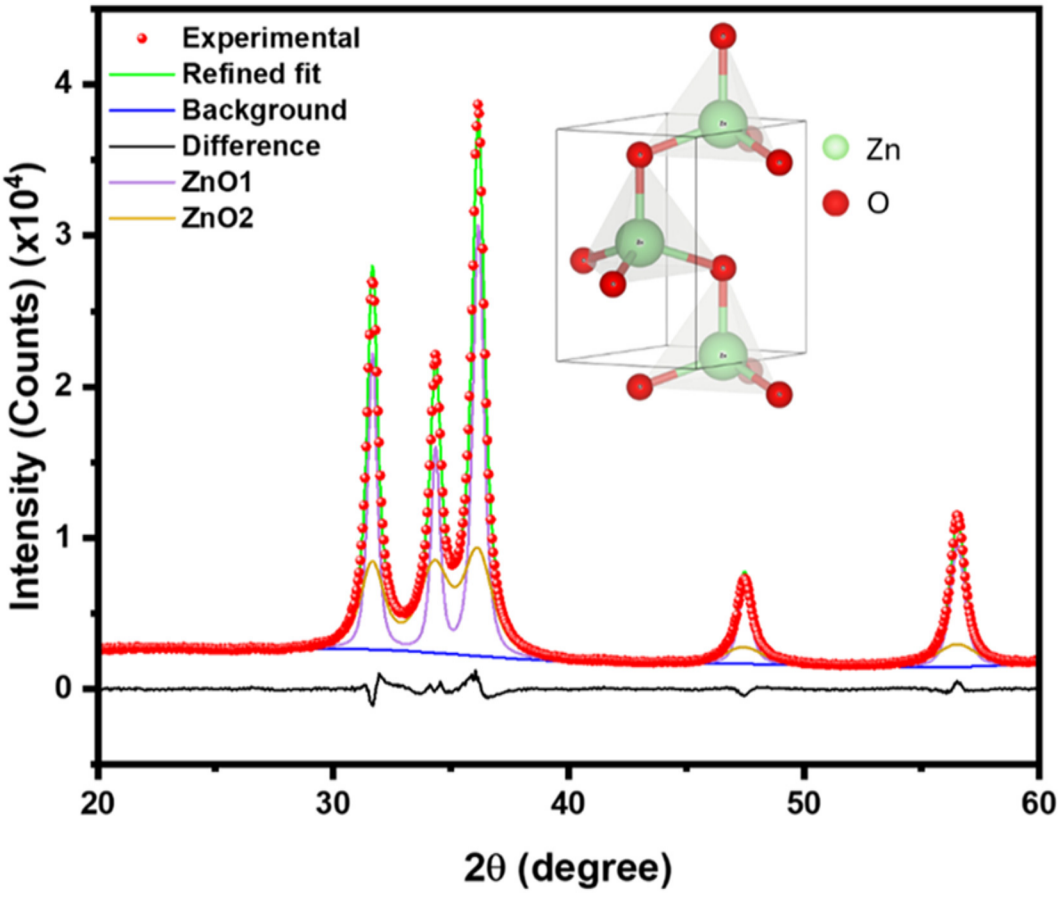

Figure 2. Rietveld refinement of the ZnO XRD data using bimodal function Profex.

Rietveld refinement (Table 1) renders a higher average crystallite size (26 nm and 47 nm) as compared to both the Scherer estimate and the Williamson–Hall approach

(11.8 ± 0.9 nm and 9.88 nm, respectively). Notably, these large crystallite sizes are comparable with the average NP size estimated from scanning electron microscopy images (see below). This might indicate that a fraction of the NP distribution is composed of single crystal particles, whereas the rest represents polycrystalline NPs. Furthermore, although of the same order of magnitude, microcrystalline strain obtained from Rietveld refinement (~4.5×10^{-3}) is also higher than the one estimated by the Williamson–Hall method (1.5×10^{-3}). These differences are related to different underlying assumptions and should be considered within the scope of specific settings and method limitations.

Table 1. Crystal parameters and Rietveld refinement statistics for the ZnO NP sample.

Phase	Crystal Parameters (nm)		Crystallite Size (nm)	Microcrystalline Strain (ε) (10^{-4})	Refinement Statistics			
	a	c			Rexp	Rwp	χ^2	GOF
ZnO1 (47%)	0.325	0.520	47	42	1.62	2.46	2.30	1.5
ZnO2 (53%)	0.325	0.521	26	51				

3.1.2. UV-Visible Spectroscopy

The surface plasmon resonance (SPR) band of ZnO NPs typically appears in UV-Vis spectra as a characteristic absorption peak between 310 and 380 nm [18]. Figure 3 shows the UV-Vis absorption spectrum of the ZnO NPs within the wavelength range of 200 to 850 nm, with a prominent absorption maximum at 321 nm. The biosynthesized ZnO NPs exhibit strong intrinsic absorption in the ultraviolet region (λ < 400 nm) and weak absorption in the visible region (λ > 400 nm). ZnO is a wide bandgap semiconductor, and the UV absorption arises from direct electronic transitions between the valence band (primarily O 2p orbitals) and the conduction band (Zn 4s orbitals).

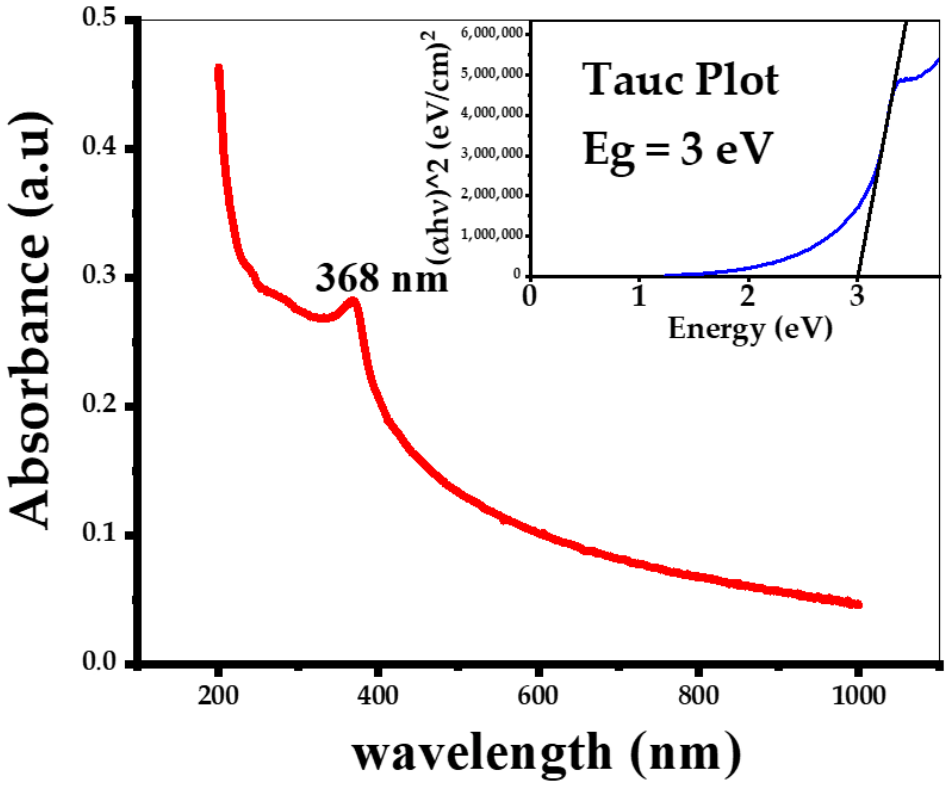

Figure 3. UV-Vis absorption spectra of the biosynthesized ZnO NPs. The inset shows the Tauc plot used to determine the optical band gap (E_g).

From the experimental UV-Vis spectra, the Tauc–Wood method was used to estimate the ZnO NPs band gap (E_g). The E_g value was obtained by a linear extrapolation of the $(\alpha h\nu)^2$ versus $h\nu$ plot (Tauc plot), yielding an estimated band gap of 3.0 eV, which is within the range of previously determined optical band gaps for ZnO NPs [17–19] and is slightly higher than that of bulk ZnO (E_g = 3.37 eV). Although the Tauc plot method has certain limitations—such as absorption tails, quantization effects, spectral overlap of different bands, excitons/many-body effects, and optical transitions via localized charge carriers [22], it remains widely used due to its simplicity. Previous studies of bioengineered ZnO NPs reported optical band gaps estimated using Tauc plots in the range of 2.75–4.1 eV [23,24]. Based on these data, UV irradiation is expected to efficiently excite the ZnO NPs.

3.1.3. Results of SEM and EDS Analyses

The size and morphology of the ZnO NPs synthesized using annatto plant leaf extracts were examined by SEM (Figure 4a,b). The images were recorded at magnifications corresponding to scales of 5 µm and 500 nm, respectively, revealing that the ZnO NPs are agglomerated. The agglomerates consist of ZnO NPs clustered together (Figure 4a,b). SEM images also (Figure 4a,b) show that the ZnO NPs exhibit a nearly spherical morphology, which is commonly encountered for biosynthesized ZnO NPs [25,26].

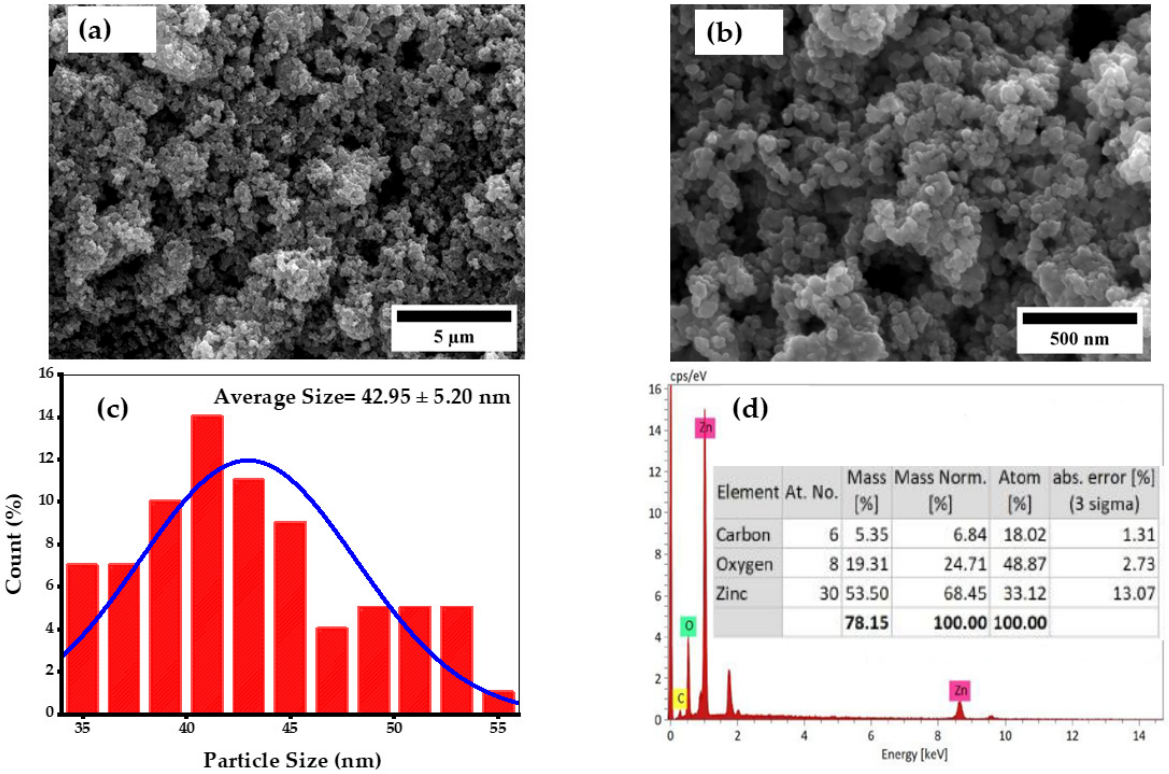

Figure 4. SEM characterization of biosynthesized ZnO NPs: (**a**) low-magnification image; (**b**) high-magnification image; (**c**) particle size distribution; and (**d**) energy-dispersive X-ray spectroscopy (EDS) analysis.

To estimate an average particle size (Figure 4c), high-magnification SEM images were analyzed. The diameters of 200 individual NPs were measured and statistically analyzed using ImageJ 1.54 g software, resulting in a size range of 35–55 nm and an average diameter of 43 ± 5 nm. The observed NP agglomeration can be attributed to the high specific surface area of the nanoparticles, which promotes clustering [27]. It is well documented that a commercial-grade zinc oxide has a surface area range of 2.5 to 12 m^2/g, while nanoparticle zinc oxide can have much higher surface areas [28]. Indeed, ZnO nanoparticles obtained

from zinc nitrate hexhydrate $Zn(NO_3)_2.6H_2O$ via a precipitation route with sodium carbonate Na_2CO_3 in water had surface areas between 25.36 and 8.78 m^2/g, depending on the annealing temperature [29]. At the same time, the mesoporous ZnO nanoparticles prepared using the sol-gel method were reported to have a specific surface area ranging between 50.41 m^2/g and, quite impressively, 578 m^2/g [30]. Similar high surface areas were reported for green-synthesized nanoparticles. For example, BET analysis of ZnO nanoparticles synthesized using *Peganum harmala* seed extract revealed a specific surface area of 442 m^2/g [31]. ZnO NPs synthesized utilizing *Canna indica* L. leaf extract exhibited a very high BET surface area of 718.7 m^2/g [32], whereas green ZnO NPs derived from red seaweed (*Pterocladia capillacea*) had a BET surface area of 113.751 m^2/g [33]. All this evidence is consistent with a high surface area expected for NPs, favoring their clustering and aggregation, which depends on their morphology and conditions of synthesis [34].

Comparison of the particle size obtained from SEM average crystallite size XRD estimates indicates that the SEM-observed particles are mostly polycrystalline; however, a fraction of NPs can be monocrystalline (see above).

NP aggregation has an impact on their photocatalytic properties [35], and therefore, below we have investigated dye photocatalytic degradation using ZnO NPs biosynthesized with annatto tree leaf extract. Furthermore, nanoparticle shape plays a crucial role in their antibacterial activity [36]. In particular, spherical nanoparticles are known to exhibit strong antibacterial properties [37], as their high surface-to-volume ratio enhances interactions with bacterial membranes.

Finally, EDS analysis was performed to determine the elemental composition of the ZnO NPs (Figure 4d). The EDS analyses confirmed the presence of two main elements, zinc (Zn) and oxygen (O). The atomic and weight percentages of Zn and O were 33.12% (68.45%) and 24.71% (48.87%), respectively. A small fraction of carbon was also detected, likely originating from residual organic compounds from the annatto tree leaf extract that remained in the samples after sintering.

3.1.4. FT-IR Spectroscopy Evaluation

In line with the EDS analysis, the contribution of functional groups from the phytochemicals present in the plant extract used for the synthesis of ZnO NPs was also identified via FT-IR analysis (Figure 5). The broad band centered around 3500 cm^{-1} in the FT-IR spectrum can be attributed to strong stretching vibrations of hydroxyl groups (−OH) present in phenolic compounds and flavonoids from the annatto plant leaf extract. A less intense peak at 1620 cm^{-1} arises from the stretching vibrations of C=C double bonds encountered in alkenes and aromatic compounds [38]. Similarly, the peaks observed at 1400 cm^{-1} and 1050 cm^{-1} can be associated with C-O stretching modes [39]. Additionally, the strong band around 550 cm^{-1} can be attributed to the stretching vibrations of Zn–O bonds, confirming the successful formation of ZnO NPs [40].

3.1.5. Point of Zero Charge (pH_{pzc}) Measurements

The point of zero charge (pH_{pzc}) is reached when the positive and negative charges on the surface of a nanoparticle are equal. Analysis of Figure 6 shows that ZnO NPs pH_{pzc} = 8.73. This means that, when the pH of the solutions is higher than the pH_{pzc}, the dominant charge of the NP surface will be negative. On the other hand, when the value of the pH solution is lower than pH_{pzc}, the predominant charge of the surface will be positive [41]. This has impacts on the interactions between the NPs and dyes and thus the photocatalytic degradation of dyes [13–23]. This phenomenon was further investigated in dye photocatalytic degradation studies (see below).

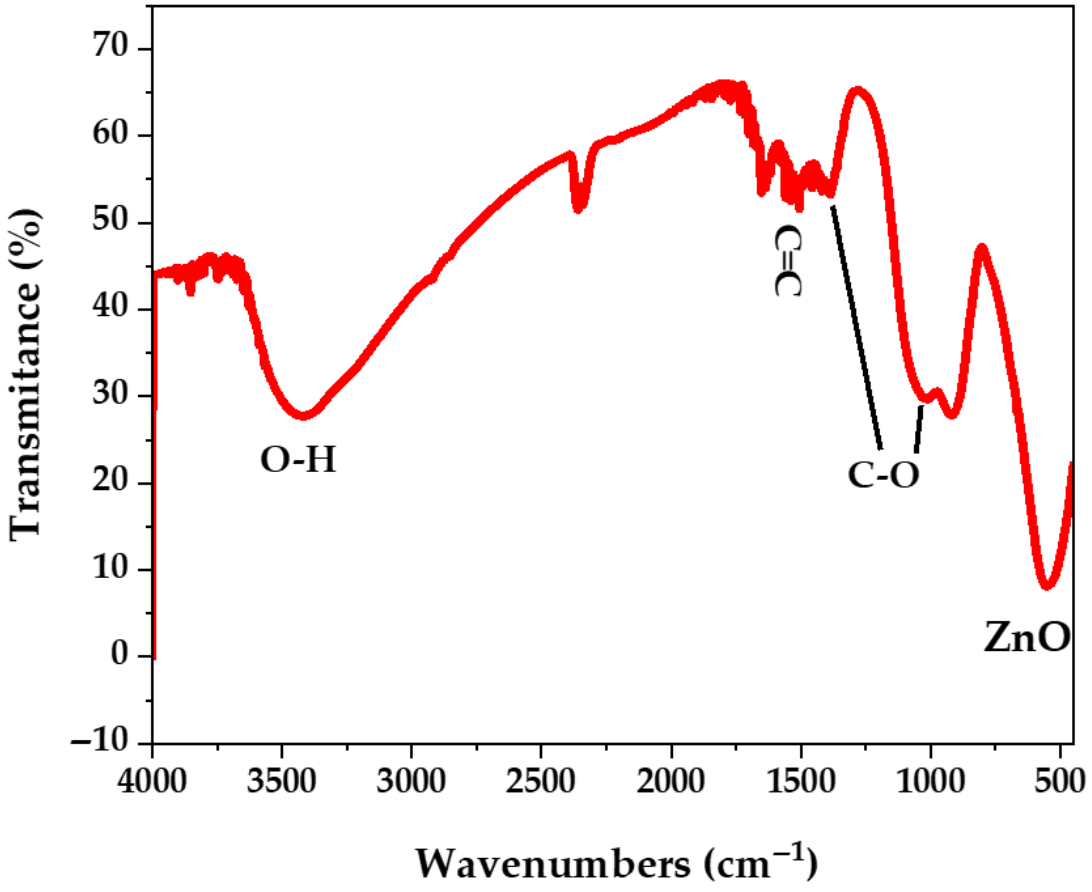

Figure 5. IR spectra of the bioengineered ZnO NPs using annatto tree leaf extract.

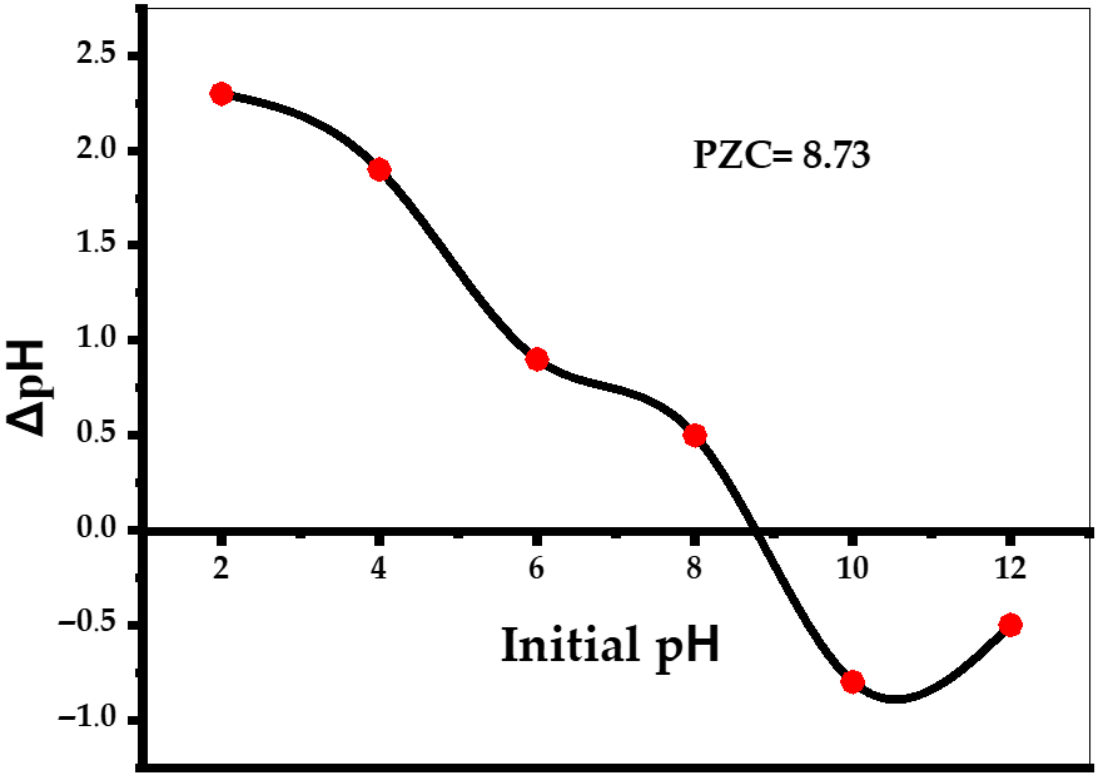

Figure 6. The point of zero charge (pzc) plot for the ZnO nanoparticles biosynthesized using annatto leaf extract.

3.1.6. Thermogravimetric Analysis (TGA)

The thermal behavior of the nanoparticles up to 1000 °C was evaluated by TGA under both N_2 and air atmospheres. In both cases, a relatively steep transition at approximately 200 C, corresponding to about 2.5% of mass loss, is observed, followed by a featureless, slow descent up to around 800 °C, where a second transition occurs. The first transition is most likely related to the evaporation of water molecules physically adsorbed on the ZnO NPs, whereas the second weight loss may be attributed to the removal of residual organic material, CO_2 desorption from the material surface, and the reorganization of the ZnO NPs. It can be observed that the transition in the absence of oxygen (Figure 7a) is considerably sharper than in the air atmosphere. At the same time, total mass loss in the air (10.45%, Figure 7b) is higher than under a nitrogen atmosphere (8.55%, Figure 7a), which is most probably related to oxidation of the organic matter attached to the NPs.

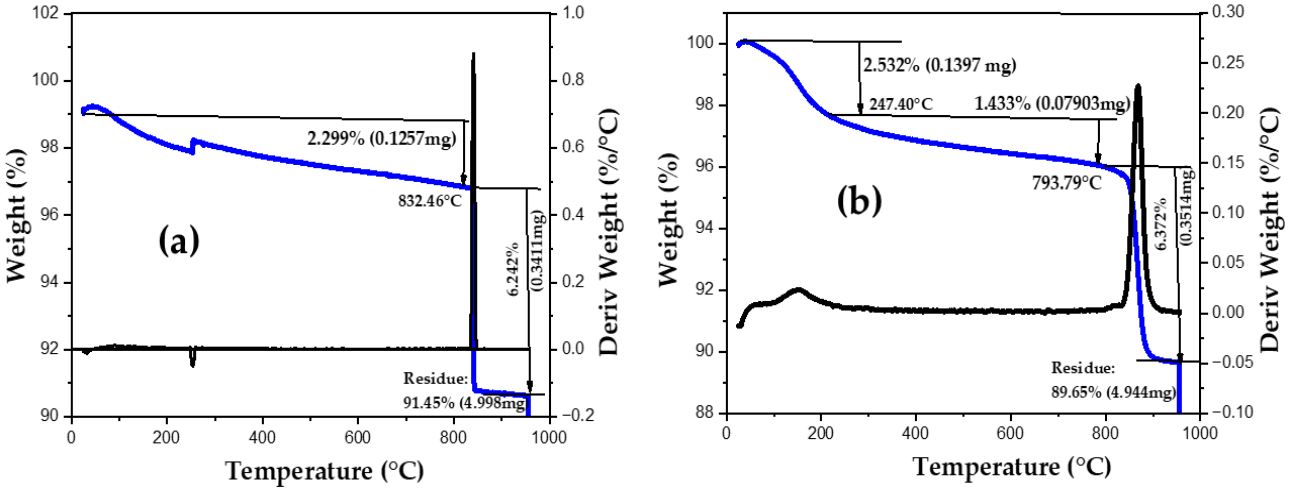

Figure 7. Thermogravimetric analysis of ZnO NPs biosynthesized using annatto tree leaf extract in the atmosphere of (**a**) N_2 and (**b**) Air.

3.2. ZnO Nanoparticles Photocatalytic Activity

The photocatalytic degradation properties of the biosynthesized ZnO nanoparticles were evaluated in the photodegradation of MB dye. A change in the maximum absorption in UV-Vis spectra as a function of UV irradiation time is shown in Figure 8a. The photocatalytic degradation of MB under UV irradiation in the presence of ZnO NPs was initially performed without adjustment of pH for the MB dye with an initial concentration of 5 ppm and 25 mg of ZnO catalyst for a period of 7 h. It is evident from Figure 8a that there is a gradual decrease in the peak (λmax = 663 nm) with increasing the light irradiation time. The gradual decrease in the UV-Vis intensities might be due to the adsorption of dye particles on the active sites of the ZnO photocatalyst. The catalytic degradation of MB dye solution in the presence of ZnO NPs was also quantified by the ratio, Ct/C_0, where C_0 and Ct correspond to the initial and final concentrations of MB dye solution. Figure 8b shows the comparison of changes in the Ct/C0 ratio vs. time. After seven hours of UV light exposure, 70% of the MB dye was photodegraded (Figure 8c). The kinetic studies of photocatalytic degradation of MB dye over the synthesized ZnO NPs photocatalyst under UV light (Figure 8d) displayed that the photocatalytic degradation process occurs through the Langmuir–Hinshelwo pseudo-first-order reaction according to the following Equation:

$$\ln\frac{C}{C_0} = -k_1\, t$$

where C_0, C, and k_1 represent the initial concentration of MB dye, the concentration of MB dye at time t, and the observed pseudo-first-order rate coefficient, respectively. The plots of $\ln(C/C_0)$ for the pseudo-first-order are shown in Figure 8d. The MB photodegradation rate constants of 0.16501 h^{-1} have accomplished under UV light.

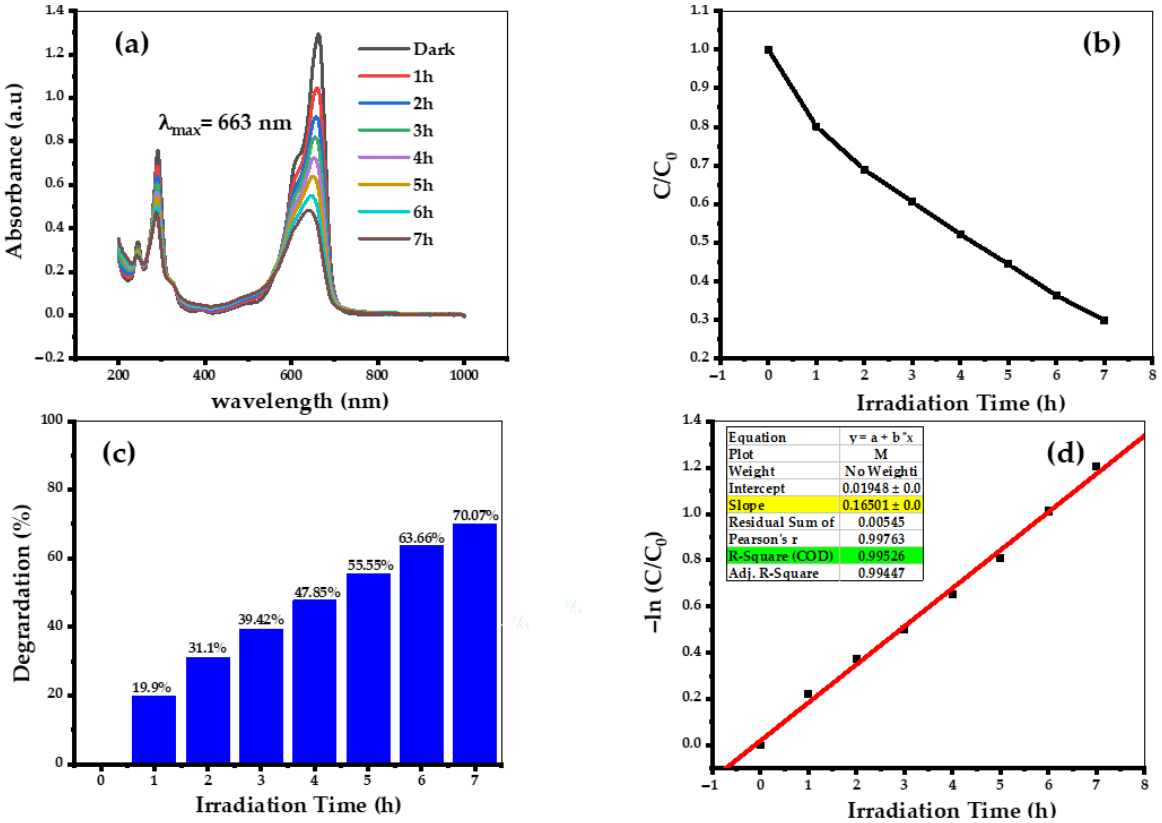

Figure 8. (**a**) MB dye absorption spectra using green synthesized ZnO NPs under UV light source. (**b**) Ratios (C/C_0). (**c**) The degradation efficiency and (**d**) the plots of $\ln(C/C_0)$ versus irradiation time.

3.3. pH Optimization of the Photocatalytic Reaction

Photocatalysis can be applied, for example, to remove poorly biodegradable and/or organic substances from wastewater. In this process, organic dyes can be completely degraded or eventually reach an efficiency endpoint. In this study, we investigated the temporal evolution of the absorbance spectra during a photocatalytic experiment using ZnO NPs for the degradation of a 5 mg/L methylene blue (MB) solution at three different pH values and compared them with the same process in the absence of nanoparticles (negative control experiments).

Figure 9 demonstrates strong dye degradation promoted by ZnO NPs at pH 10 and pH 12, reaching 71.24% and 95.27% removal, respectively, after 110 min of UV light exposure. At pH 8, a much lower degree of dye degradation is observed over the 110 min period, resulting in only approximately 8.35% degradation. In the absence of ZnO NPs, the degradation is very small for all the pH values, demonstrating a crucial role of ZnO NPs in this catalysis. At pH = 8, the surface of the nanoparticles becomes slightly positively charged, which repels the cationic MB dye, thereby reducing adsorption and negatively impacting photodegradation efficiency. In contrast, at pH 10 and pH 12, the ZnO surface becomes negatively charged, enhancing electrostatic attraction with the positively charged MB molecules, which leads to their stronger interactions with the ZnO NPs and more efficient photodegradation.

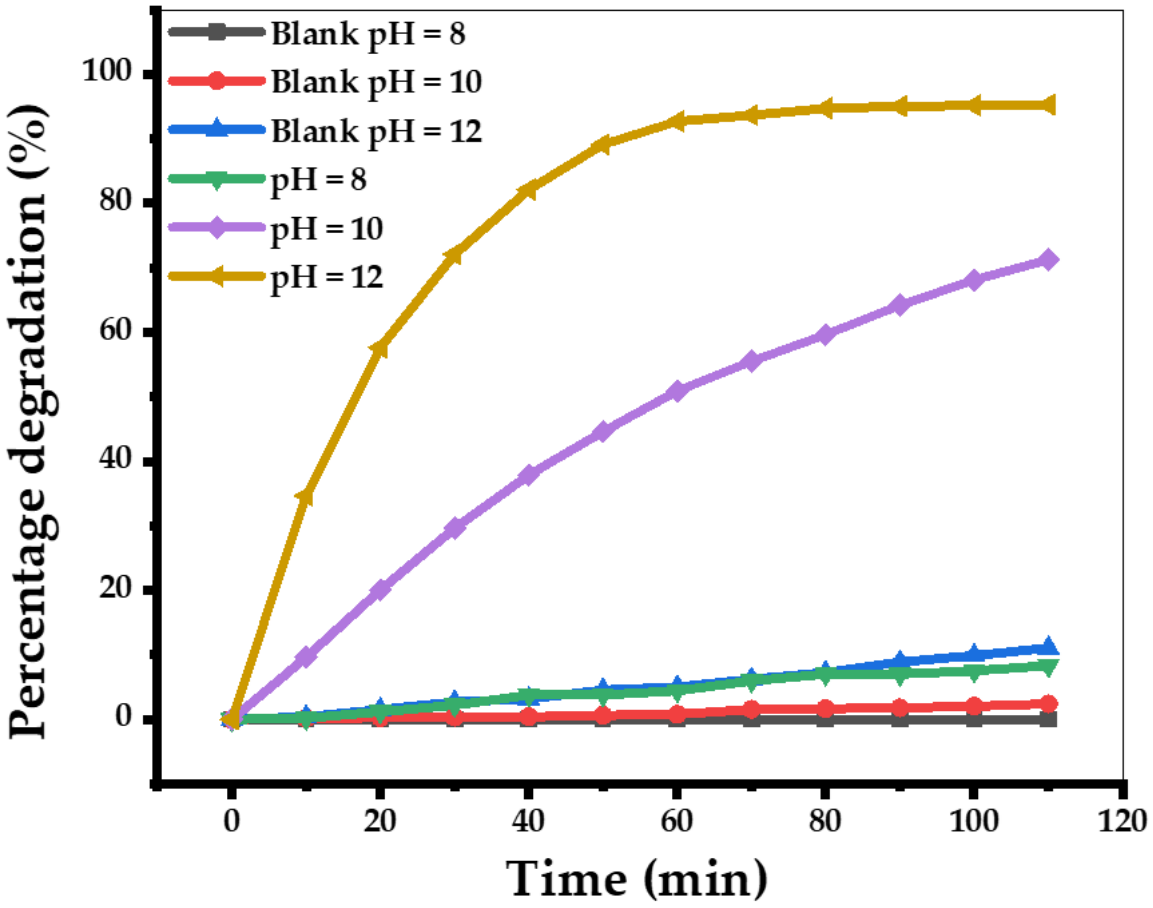

Figure 9. Photodegradation of methylene blue (MB) by ZnO NPs biosynthesized with annatto tree leaf extract at different pH values.

It is informative to compare the experimentally observed photocatalytic efficiency using photoactivated biogenic ZnO NPs with the photocatalytic efficiencies reported in the literature (Table 2).

Table 2. Photodegradation efficiencies of various plant-based biogenic ZnO NPs.

/	Plant Extract	Bandgap, eV	Light Source/Time	Dye/Antibiotic	Efficiency	References
ZnO (quasi-spherical)	Annatto plant leaves	3.0	UV, 110 min	Methylene blue (MB), 5 mg/mL	95.27%	Current study
ZnO (spherical)	Coffee leaves	3.2	UV, 120 min	Methylene blue (MB), 5 mg/mL	70%	[13]
ZnO (spherical)	Oiti leaves	2.75	UV, 120 min	Crystal violet (CV)	79%	[23]
ZnO (quasi-hexagonal)	*Alchornea laxiflora* leaves	2.50–3.67	Sunlight 60 min	Congo red (CR) dye, 1.5 mg/L	87%	[42]
ZnO (spherical and hexagonal)	Pullulan	3.3	UV, 120 min	Amoxicillin (AMX) and paracetamol (PCT) 30 ppm	85.7% and 96.8% for AMX and PCT	[43]
ZnO (nanorods)	Garlic bulbs (*Allium sativum*)	3	Sunlight, 150 min	Methylene blue (MB), 10 ppm	96%	[44]
ZnO (flower like shape)	*Euphorbia sanguinea*	2.72–4.37	Sunlight, 60 min	Malachite green dye, 1.5 mg/L	92%	[45]
ZnO (Spherical and hexagonal)	*Actinidia deliciosa* (kiwi) fruit peel	3.06	UV, 120 min	p-bromophenol 15 mg/L	96.3%	[46]

Table 2. *Cont.*

/	Plant Extract	Bandgap, eV	Light Source/Time	Dye/Antibiotic	Efficiency	References
ZnO (semi-spherical)	*Justicia spicigera*	3.3	UV, 120 min	Methylene blue (MB), 15 mg/L	90%	[47]
ZnO (Sphere and hexagonal)	Pomegranate, beetroot, and seder	2.84, 2.63 and 2.59	UV, 270 min	Methyl orange MO, 50 mg/L	32%, 87%, and 52%	[48]

It is clear that the experimentally observed photodegradation efficiency achieved in the current study is equal to or superior to the efficiencies achieved previously with different types of pollutants and light sources (Table 2). This highlights the high quality of biogenic ZnO NPs produced with annatto tree leaf extract in photodegradation applications.

3.4. ROS Scavenging Experiments

The most important reactive oxygen species involved in the breakdown of organic compounds should be identified in order to shed light on a photocatalytic process utilizing ZnO. When MB is photodegraded using ZnO, four different radical scavengers, ethylenediaminetetraacetic acid (EDTA), dimethyl sulfoxide (DMSO), para-benzoquinone (BQ), and Isopropyl alcohol (IPA), can be added to capture the roles of photogenerated holes (h^+), electrons (e^-), superoxide radicals ($O_2\bullet^-$), and hydroxyl radicals (•OH), respectively, in photocatalytic process [49,50]. All scavengers but BQ were tested at the same concentration (1.0 mM), with 5 ppm of aqueous MB solution at pH = 12 and using 25 mg of ZnO catalyst, whereas the former scavenger was applied at 0.5 mM concentration. The plots of C/C_0 and the percentage of dye degradation in the presence and absence of scavengers are depicted in Figure 10a,b. The photodegradation efficiency of MB was significantly reduced in comparison to the absence of scavengers. EDTA, DMSO, and BQ reached only 24.1%, 26.91%, and 31.8%, respectively. At the same time, the addition of IPA had little effect, leading to 90.6% of the maximum degradation, which is close to 95.35% observed in the absence of scavengers. According to the influence of scavengers on the efficiency of MB photodegradation, their inhibitor effect is arranged as EDTA > DMSO > BQ > IPA > No scavengers. Thus, one can conclude that, while ·OH only slightly impacts the photodegradation process, h^+, e^-, and $\cdot O^{2-}$ radicals play crucial roles in the ZnO NP driven photocatalysis of MB dye.

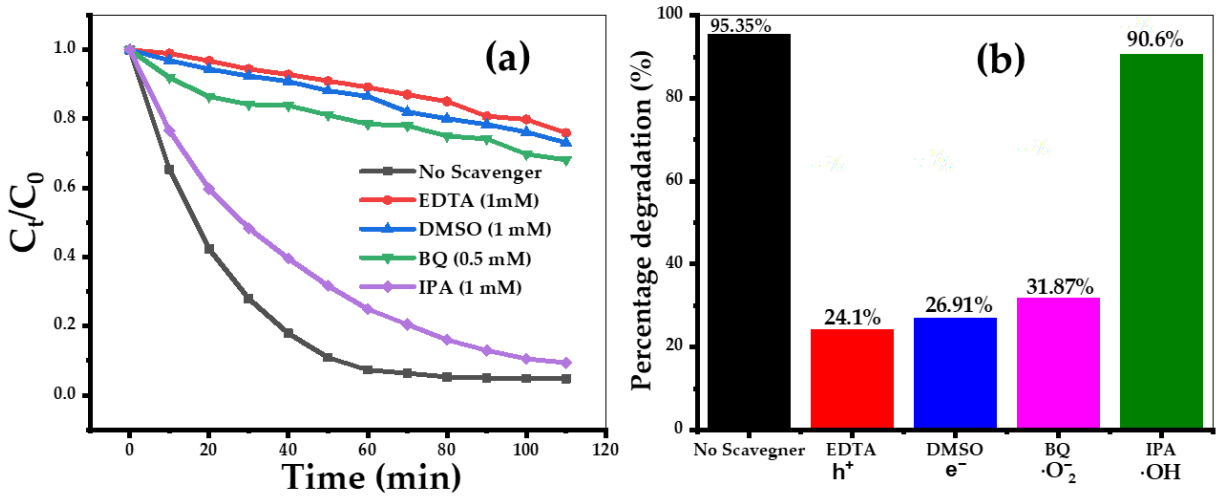

Figure 10. (**a**) Effects of adding BQ, DMSO, EDTA, and IPA during the degradation of MB dye mixture over ZnO; (**b**) the maximum percentage degradation with the different scavenging agents.

3.5. Reusability of the Photocatalyst

Next, the reusability of the biosynthesized ZnO NPs photocatalyst has also been investigated. After each cycle of the reaction, the ZnO catalyst was recovered from the reaction mixture by centrifugation, and before using it for other cycles to analyze the degradation efficiency, the ZnO catalyst was washed thoroughly with ethanol and double-distilled water to eradicate the residual dye molecules from the catalyst surface. The recovered ZnO nanophotocatalyst was reused four times in photodegradation experiments of MB dye degradation under similar experimental conditions without an apparent decrease in its photocatalytic efficiency (Figure 11). The progress of the reaction was monitored by measuring the absorbance of aliquots of the reaction solution that are taken at regular time intervals. Figure 11 reveals that the ZnO NPs have not only excellent catalytic efficiency but also remain stable after the fourth cycle and beyond. To investigate the impact of the photocatalytic process on the photocatalyst itself, we recovered the ZnO NPs at the end of the fourth cycle and subjected them to an XRD analysis. The XRD studies reveal a well-preserved crystalline structure. The dislocation constant, the microstrain, and the average size of the ZnO nanoparticles biosynthesized before and after the photocatalytic degradation were calculated from the XRD patterns and summarized in Table 3. Our results demonstrate that UV light illumination of the ZnO NPs leads to a significant increase in the average crystallite size and a decrease in the dislocation density (Table 3), presumably caused by the NPs photoannealing.

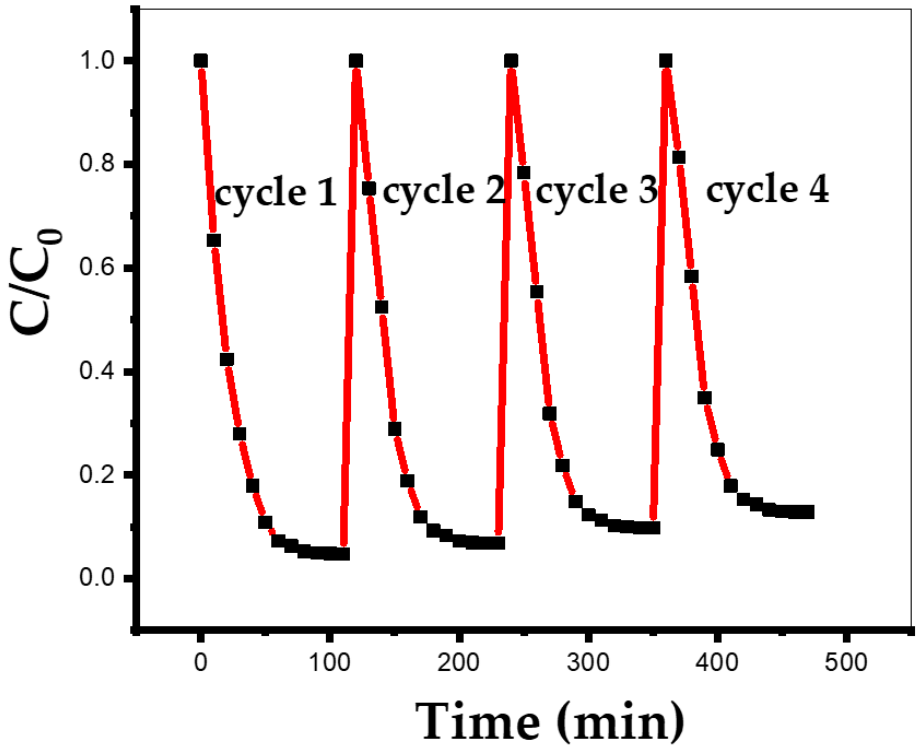

Figure 11. The reusability of the ZnO NPs.

Table 3. Average crystallite size, dislocation density, and strain for the bioengineered ZnO nanoparticles before and after 4 cycles of the photocatalytic degradation.

	Average Crystallite Size (nm)	Dislocation Density (δ) (nm^{-2})	Strain
Before	9.88	10.2×10^{-3}	1.5×10^{-3}
After	26.20	1.46×10^{-3}	1.08×10^{-3}

3.6. Antibacterial Activity of the NPs Against Microbial Pathogens

ZnO NPs are known to have excellent antibacterial activities [51,52]. Combined with their low toxicity and cost-effective production, these properties make ZnO NPs a highly promising material for antimicrobial applications [51,52]. In previous studies, the antibacterial effects of ZnO NPs have been demonstrated against both Gram-positive and Gram-negative bacteria, including *E. coli*, *P. aeruginosa*, *Staphylococcus aureus*, *Enterococcus faecalis*, *Streptococcus pyogenes*, *Vibrio cholerae*, and *Klebsiella pneumoniae*, among others [52].

Here, we applied the biosynthesized ZnO NPs to interfere with the growth of *E. coli*, *P. aeruginosa*, and *S. enterica*. The NPs were able to inhibit the growth of the waterborne pathogens *E. coli*, *P. aeruginosa*, and *S. enterica* at concentrations ranging from 0.312 to 2.5 mg/mL (Table 4). For comparison, we also used ZnO nanoparticles biosynthesized using coffee leaf extract, as described previously [13], which also demonstrated excellent antimicrobial properties (Table 4). This indicates a possibility of their applications as water decontaminating agents. Although, at first glance, these concentrations may appear somewhat high for water decontamination purposes, it is important to keep in mind that these NPs are easy to produce using the environmentally friendly approach. More precise evaluation of the economic viability of water treatment using the biosynthesized ZnO NPs should involve a detailed cost analysis under specific settings.

Table 4. Minimum Inhibitory Concentrations for the two biosynthesized nanoparticles (using annatto tree and/or coffee leaf extracts) against different microbial pathogens.

Microrganism	MIC of ZnO NP Synthesized Using Annatto Tree Leaf Extract (mg/mL)	MIC of ZnO NP Obtained Using Coffee Leaf Extract (mg/mL)
E. coli ATCC 25922	2.5	1.25
P. aeruginosa ATCC 27853	0.312	0.312
S. enterica serovar Thyphimurium ATCC 14028	2.5	2.5

3.7. Insights into Putative Molecular Mechanisms of the ZnO NPs Bacterial Toxicity

One of the proposed mechanisms of ZnO nanoparticles' antibacterial activity, reported in the literature, involves the generation of reactive oxygen species (ROS) [51,52]. Therefore, we evaluated the ability of ZnO nanoparticles synthesized using annatto and coffee extracts to generate intracellular reactive oxygen species (ROS), as well as singlet oxygen in a cell-free system. As shown in Figures 11 and 12, both singlet oxygen and intracellular ROS were produced in statistically significant amounts by the two nanoparticles. It is important to note that the singlet oxygen indicator used in Figure 11 inherently exhibits weak basal blue fluorescence, which may be detected in the control group; however, in the presence of singlet oxygen, this indicator emits green fluorescence. In addition, for the dye employed in Figure 12, dye–dye quenching and subsequent photobleaching upon illumination may occur, leading to an apparent increase in fluorescence in control samples. To account for these effects, statistical analyses were performed, confirming that the differences between the negative control and nanoparticle-treated groups were statistically significant.

Recently, Mendes et al. (2022) [53] investigated the potential mechanism of action of ZnO NPs against *Escherichia coli*, *Staphylococcus aureus*, *Pseudomonas aeruginosa*, and *Bacillus subtilis*. The authors observed that, although the nanoparticles did not interfere with bacterial cell division, the cell membranes of all tested strains showed signs of damage after just 15 min of exposure. The authors proposed that this effect is related to the semiconductor nature of ZnO, a transition metal oxide with a wide bandgap. Upon exposure to radiation with energy exceeding the bandgap, electrons are excited to the conduction band, producing positively charged holes in the valence band. These holes

possess strong oxidizing properties and can react with water or other biomolecules, leading to the formation of reactive oxygen species (ROS). ROS are capable of disrupting key cellular processes such as protein synthesis and DNA replication. In addition to oxidative stress, membrane damage may also result from charge destabilization due to electronic excitation, as well as from the release of Zn^{2+} ions in aqueous environments. These zinc ions can further impair bacterial metabolism by inhibiting glycolytic enzymes [53].

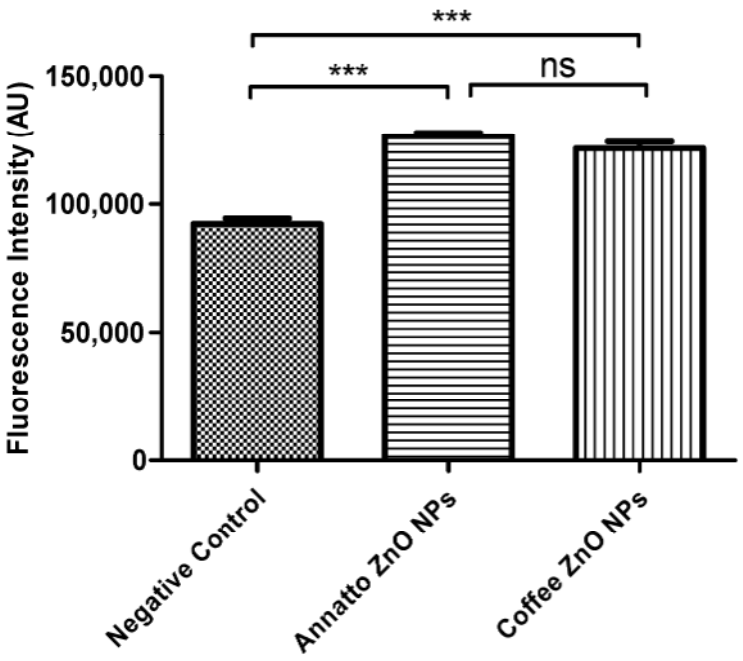

Figure 12. Quantification of singlet oxygen produced by biosynthetic ZnO NPs produced by annato tree and by coffee leaf extracts in aqueous media. Bars represent the standard deviation. ***—$p < 0.0001$; ns—nonsignificant difference. One-way ANOVA with Tukey's multiple comparisons test.

This ROS-based mechanism is highly dependent on exposure to external light of specific wavelengths, which may limit ZnO nanoparticles' antibacterial efficiency in systemic applications [54,55]. However, this limitation is not a concern for water decontamination, where light exposure can be more easily controlled, thereby highlighting an important advantage of ZnO nanoparticles for environmental applications.

The growing concerns regarding water contamination by bacterial pathogens and the spread of antimicrobial resistance [8] underscore the urgency in developing effective and sustainable water disinfection methods. In this study, we explored the biosynthesis of ZnO NPs using annatto tree and coffee leaf extracts and evaluated their antibacterial properties against common waterborne pathogens: *Escherichia coli*, *Pseudomonas aeruginosa*, and *Salmonella enterica*. The obtained results demonstrate the promising potential of biosynthesized ZnO NPs as water disinfectant agents and demonstrate that both biogenic ZnO NPs can be used for elimination of microbial pathogens.

The ZnO NPs biosynthesized with annatto leaf extract demonstrated inhibitory activity against *E. coli*, *P. aeruginosa,* and *S. enterica* at concentrations ranging from 0.312 to 2.5 mg/mL (Table 4). In comparison with ZnO NPs synthesized with coffee leaf extract [12], similar or slightly lower efficacy was observed for annatto tree leaf extract ZnO NPs against *E. coli*, but identical MICs for *P. aeruginosa* and *S. enterica*. This suggests that both plant extracts are effective in producing nanoparticles with antimicrobial properties, although the specific characteristics of the bioactive compounds in each extract may influence the final properties of the nanoparticles and their interaction with different bacterial species.

The lower MIC for *P. aeruginosa* with both nanoparticles, compared to *E. coli* and *S. enterica*, may indicate a higher sensitivity of this bacterium to the nanoparticles or differences in its virulence mechanisms or cell wall structure that make it more susceptible.

The investigation of antibacterial mechanisms confirmed that the toxicity of ZnO NPs is significantly associated with the generation of reactive oxygen species (ROS). Both singlet oxygen (Figure 12) and intracellular ROS (Figure 13) were produced in statistically significant amounts by both annatto tree and coffee leaf extract-based NPs, corroborating previous findings that point to ROS formation as one of the main mechanisms of antimicrobial action of ZnO NPs [51,52]. This process is promoted by the semiconductor nature of ZnO NPs, since their exposure to UV light, considering the 3 eV band gap, leads to electron excitation and hole formation, which react with water and other biomolecules to generate ROS. The ROS cause oxidative damage of essential cellular components, such as proteins and DNA, and can also induce cell membrane damage [53]. The release of Zn^{2+} ions in aqueous environments also contributes to bacterial toxicity by interfering with cellular metabolism [53].

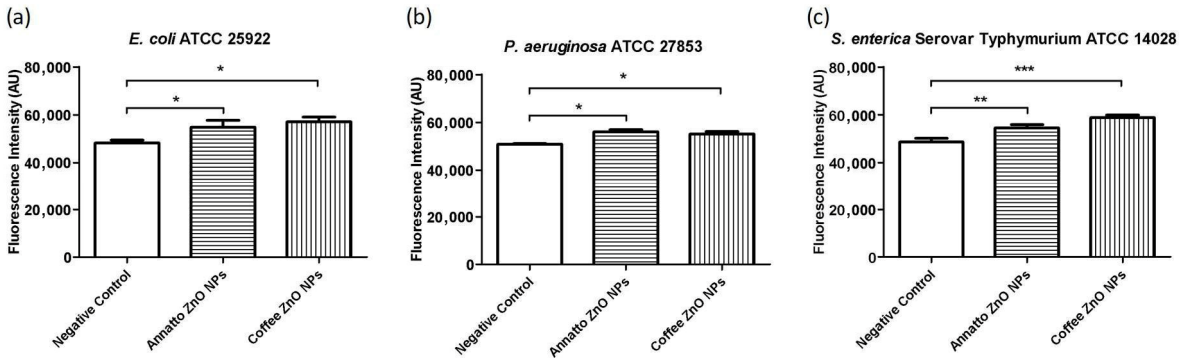

Figure 13. Quantification of intracellular reactive oxygen species produced by ZnO NPs biosynthesized using annatto tree and by coffee leaf extracts in (**a**) *E. coli* ATCC 25922, (**b**) *P. aeruginosa* ATCC 27853, and (**c**) *S. enterica* ATCC 14028. Bars represent the standard deviation. ***—$p < 0.0005$; **—$p < 0.005$; *—$p < 0.05$; ns—nonsignificant difference. One-way ANOVA with Tukey's multiple comparisons test.

The dependence of ROS generation on external light exposure [54], which can be a limitation for systemic applications, becomes an advantage in water disinfection contexts, where lighting control is feasible.

Although ZnO NPs are often considered "resistance-proof" due to their multi-factorial mode of action [12], a recent study [56] demonstrated that *S. enterica* can develop adaptations, such as membrane modifications and increased biofilm formation, after prolonged exposure to subinhibitory concentrations of ZnO NPs. These findings underscore the need for more in-depth investigations into the molecular mechanisms of action of metal-based nanoparticles and the anticipation of potential resistance pathways.

4. Conclusions

Water quality is essential for human life; therefore, the development and implementation of adequate water treatment procedures is of utmost importance. In this study, we successfully synthesized biogenic ZnO NPs with an average size of 42.95 ± 5.2 nm and a bandgap of 3 eV using annatto plant leaf extract, thoroughly characterized them using an array of analytical techniques, and applied them for both elimination of waterborne pathogens and dye photodegradation. The potential antibacterial mechanisms of the NPs were investigated, revealing statistically significant production of intracellular reactive oxygen species as well as an extracellular singlet oxygen generation. Furthermore, the

biosynthesized ZnO NPs were significantly more efficient against *Pseudomonas aeruginosa* as compared to *E. coli* and *S. enterica.* The integration of annatto tree leaf extract in the green synthesis of ZnO NPs not only improves their structural characteristic but also enhances their functional properties, making them efficient agents for dye degradation (reaching over 95% efficiency after 110 min of UV light exposure) and bacterial elimination. This eco-friendly approach to nanoparticle synthesis aligns with sustainable practices in materials science.

Author Contributions: A.d.J.B.: Investigation, Conceptualization, Methodology, Writing—original draft. A.N.G.D.: Investigation, Conceptualization, Methodology, Data curation, Writing—original draft, Writing—review and editing. V.O.A.P.: Investigation, Conceptualization, Methodology, Data curation, Writing—original draft, Writing—review and editing. M.T.: Investigation, Conceptualization, Methodology, Visualization. M.A.S.: Investigation, Methodology, Data curation. S.V.: Conceptualization, Methodology, Resources, Funding acquisition. S.D.: Investigation, Conceptualization, Methodology, Visualization. V.S.V. Conceptualization, Methodology, Resources, Funding acquisition. C.R.F.: Investigation, Methodology, Data curation, Writing—review and editing, Supervision, Validation. I.P.: Investigation, Methodology, Data curation, Writing—original draft, Writing—review and editing, Supervision, Validation, Resources, Funding acquisition. All authors have read and agreed to the published version of the manuscript.

Funding: This work was supported by the Fundação de Amparo à Pesquisa do Estado de São Paulo (FAPESP, grants #2021/08780-1 and 2024/00533-3), by the Conselho Nacional de Desenvolvimento Científico e Tecnológico (CNPq, grants #306852/2021-7 and 440180/2022-8).

Institutional Review Board Statement: Not applicable.

Informed Consent Statement: Not applicable.

Data Availability Statement: The original contributions presented in this study are included in the article. Further inquiries can be directed to the corresponding author.

Conflicts of Interest: The authors declare no conflict of interest.

References

1. Kamyab, H.; Chelliapan, S.; Hayder, G.; Yusuf, M.; Taheri, M.M.; Rezania, S.; Hasan, M.; Yadav, K.K.; Khorami, M.; Farajnezhad, M.; et al. Exploring the potential of metal and metal oxide nanomaterials for sustainable water and wastewater treatment: A review of their antimicrobial properties. *Chemosphere* **2023**, *335*, 139103. [CrossRef]
2. De Mel, S.; Gruenler, J.; Khoury, L.; Heynes, A.; Fazekas, J.; Damaske, K.; Galbadage, T.; Gunasekera, R.S.; Anderson, R.S. Green synthesis of silver nanoparticles using *Magnolia alba* leaf extracts and evaluating their antimicrobial, anticancer, antioxidant, and photocatalytic properties. *Sci. Rep.* **2025**, *15*, 23709. [CrossRef]
3. Ashraf, A.; Ijaz, M.U.; Muzammil, S.; Nazir, M.M.; Zafar, S.; Zihad, S.N.K.; Uddin, S.J.; Hasnain, S.; Nayak, A.K. The role of bixin as antioxidant, anti-inflammatory, anticancer, and skin protecting natural product extracted from *Bixa orellana* L. *Fitoterapia* **2023**, *169*, 105612. [CrossRef]
4. Meng, S. Photocatalytic materials and photocatalytic reactions. *Molecules* **2025**, *30*, 269. [CrossRef] [PubMed]
5. Some, S.; Mondal, R.; Mitra, D.; Jain, D.; Verma, D.; Das, S. Microbial pollution of water with special reference to coliform bacteria and their nexus with environment. *Energy Nexus* **2021**, *1*, 100008. [CrossRef]
6. Palma, L.; Hatam, F.; Di Nardo, A.; Prévost, M. Contaminations in water distribution systems: A critical review of detection and response methods. *Aqua—Water Infrastruct. Ecosyst. Soc.* **2024**, *73*, 1285–1302. [CrossRef]
7. Iyer, V.A.; Dahiya, P.; Kumar, D. Advancements in human health risk, detection and bioremediation of bacterial contaminants in water: A review. *Phys. Chem. Earth Parts A/B/C* **2025**, *140*, 103990. [CrossRef]
8. Singh, A.; Pratap, S.G.; Raj, A. Occurrence and dissemination of antibiotics and antibiotic resistance in aquatic environment and its ecological implications: A review. *Environ Sci Pollut Res.* **2024**, *31*, 47505–47529. [CrossRef] [PubMed]
9. Zhou, Z.; Shuai, D. Disinfection and post-disinfection conditions drive bacterial and viral evolution across the environment and host. *J. Hazard. Mater.* **2024**, *474*, 134811. [CrossRef] [PubMed]
10. Li, D.; Zeng, S.; He, M.; Gu, A.Z. Water disinfection byproducts induce antibiotic resistance-role of environmental pollutants in resistance phenomena. *Environ. Sci. Technol.* **2016**, *50*, 3193–3201. [CrossRef] [PubMed]

11. Dimapilis, E.A.S.; Hsu, C.S.; Mendoza, R.M.O.; Lu, M.C. Zinc oxide nanoparticles for water disinfection. *Sustain. Environ. Res.* **2018**, *28*, 47–56. [CrossRef]
12. Sánchez-López, E.; Gomes, D.; Esteruelas, G.; Bonilla, L.; Lopez-Machado, A.L.; Galindo, R.; Cano, A.; Espina, M.; Ettcheto, M.; Camins, A.; et al. Metal-based nanoparticles as antimicrobial agents: An overview. *Nanomaterials* **2020**, *10*, 292. [CrossRef] [PubMed]
13. de Oliveira Arnoldi Pellegrini, V.; de Jesus Bernardo, A.; Rossi, B.R.; Leite, R.R.; Possatto, J.F.; Dabul, A.N.G.; Fontana, C.R.; Dlamini, Z.W.; Mahule, T.S.; Mosepele, B.Q.; et al. Antimicrobial, photodegradation and BioReRAM applications of multifaceted green zinc oxide nanoparticles synthesized using coffee leaves extract. *Sci. Rep.* **2025**, *15*, 29054. [CrossRef]
14. Monshi, A.; Foroughi, M.R.; Monshi, M.R. Modified Scherrer equation to estimate more accurately nano-crystallite size using XRD. *World J. Nano Sci. Eng.* **2012**, *2*, 154–160. [CrossRef]
15. Zak, A.K.; Majid, W.A.; Abrishami, M.; Yousefi, R. X-ray analysis of ZnO nanoparticles by Williamson–Hall and size–strain plot methods. *Solid State Sci.* **2011**, *13*, 251–256. [CrossRef]
16. Doebelin, N.; Kleeberg, R. Profex: A graphical user interface for the Rietveld refinement program BGMN. *J. Appl. Crystallogr.* **2015**, *48*, 1573–1580. [CrossRef]
17. Costa, P.; Gomes, A.T.P.C.; Braz, M.; Pereira, C.; Almeida, A. Application of the resazurin cell viability assay to monitor *Escherichia coli* and *Salmonella typhimurium* inactivation mediated by phages. *Antibiotics* **2021**, *10*, 974. [CrossRef]
18. Morkoç, H.; Özgür, Ü. *Zinc Oxide: Fundamentals, Materials and Device Technology*; John Wiley & Sons: Hoboken, NJ, USA, 2018.
19. Patterson, A.L. The Scherrer formula for X-ray particle size determination. *Phys. Rev. B* **1939**, *56*, 978–982. [CrossRef]
20. Salah, M.; Azizi, S.; Boukhachem, A.; Khaldi, C.; Amlouk, M.; Lamloumi, J. Rietveld refinement of X-ray diffraction, impedance spectroscopy and dielectric relaxation of Li-doped ZnO-sprayed thin films. *Appl. Phys. A* **2019**, *125*, 615. [CrossRef]
21. Liu, H.; Ding, Y.; Somayazulu, M.; Qian, J.; Shu, J.; Häusermann, D.; Mao, H.K. Rietveld refinement study of the pressure dependence of the internal structural parameter u in the wurtzite phase of ZnO. *Phys. Rev. B—Condens. Matter Mater. Phys.* **2005**, *71*, 212103. [CrossRef]
22. Klein, J.; Kampermann, L.; Mockenhaupt, B.; Behrens, M.; Strunk, J.; Bacher, G. Limitations of the Tauc plot method. *Adv. Funct. Mater.* **2023**, *33*, 2304523. [CrossRef]
23. Thiam, M.; Bernardo, A.d.J.; Pellegrini, V.d.O.A.; Possatto, J.F.; Dlamini, Z.W.; Mahule, T.S.; Ngom, B.D.; Mosepele, B.Q.; Thema, F.T.; Mamba, B.B.; et al. Green Synthesis of ZnO Nanoparticles Using *Licania tomentosa* Benth (Oiti) Leaf Extract: Characterization and Applications for the Photocatalytic Degradation of Crystal Violet Dye. *Processes* **2025**, *13*, 880. [CrossRef]
24. Erat, S.; Braun, A.; Çetinkaya, S.; Yildirimcan, S.; Kasapoğlu, A.E.; Gür, E.; Harputlu, E.; Ocakoglu, K. Solution-Processable Growth and Characterization of Dandelion-like ZnO: B Microflower Structures. *Crystals* **2021**, *12*, 11. [CrossRef]
25. Verma, L.M.; Kumar, A.; Bashir, A.U.; Gangwar, U.; Ingole, P.P.; Sharma, S. Phase controlled green synthesis of wurtzite (P 63 mc) ZnO nanoparticles: Interplay of green ligands with precursor anions, anisotropy and photocatalysis. *Nanoscale Adv.* **2023**, *6*, 155–169. [CrossRef] [PubMed]
26. Faisal, S.; Jan, H.; Shah, S.A.; Shah, S.; Khan, A.; Akbar, M.T.; Rizwan, M.; Jan, F.; Wajidullah; Akhtar, N.; et al. Green synthesis of zinc oxide (ZnO) nanoparticles using aqueous fruit extracts of Myristica fragrans: Their characterizations and biological and environmental applications. *ACS Omega* **2021**, *6*, 9709–9722. [CrossRef] [PubMed]
27. Narayana, A.; Bhat, S.A.; Fathima, A.; Lokesh, S.V.; Surya, S.G.; Yelamaggad, C.V. Green and low-cost synthesis of zinc oxide nanoparticles and their application in transistor-based carbon monoxide sensing. *RSC Adv.* **2020**, *10*, 13532–13542. [CrossRef] [PubMed]
28. Raja, P.M.V.; Barron, A.R. BET Surface Area Analysis of Nanoparticles. *OpenStax*. 2011. Available online: https://chem.libretexts.org/Bookshelves/Analytical_Chemistry/Physical_Methods_in_Chemistry_and_Nano_Science_(Barron)/02%3A_Physical_and_Thermal_Analysis/2.03%3A_BET_Surface_Area_Analysis_of_Nanoparticles (accessed on 13 December 2025).
29. Ismail, M.A.; Taha, K.K.; Modwi, A.; Khezami, L. ZnO nanoparticles: Surface and X-ray profile analysis. *J. Ovonic Res.* **2018**, *14*, 381–393.
30. Jadhav, N.A.; Singh, P.K.; Rhee, H.W.; Bhattacharya, B. Effect of variation of average pore size and specific surface area of ZnO electrode (WE) on efficiency of dye-sensitized solar cells. *Nanoscale Res. Lett.* **2014**, *9*, 575. [CrossRef]
31. Fazlzadeh, M.; Khosravi, R.; Zarei, A. Green synthesis of zinc oxide nanoparticles using *Peganum harmala* seed extract, and loaded on *Peganum harmala* seed powdered activated carbon as new adsorbent for removal of Cr (VI) from aqueous solution. *Ecol. Eng.* **2017**, *103*, 180–190. [CrossRef]
32. Tran, G.T.; Nguyen, T.T.T.; Nguyen, D.T.C.; Van Tran, T. Green Synthesis of ZnO Nanoparticles and Conversion of Post-extraction Residue of *Canna indica* L. Leaf into ZnO/Activated Carbon to Remove Malachite Green from Water. *Arab. J. Sci. Eng.* **2024**, *50*, 14563–14577. [CrossRef]

33. Mansour, A.T.; Alprol, A.E.; Khedawy, M.; Abualnaja, K.M.; Shalaby, T.A.; Rayan, G.; Ramadan, K.M.A.; Ashour, M. Green synthesis of zinc oxide nanoparticles using red seaweed for the elimination of organic toxic dye from an aqueous solution. *Materials* **2022**, *15*, 5169. [CrossRef]
34. Zhou, D.; Keller, A.A. Role of morphology in the aggregation kinetics of ZnO nanoparticles. *Water Res.* **2010**, *44*, 2948–2956. [CrossRef] [PubMed]
35. Jassby, D.; Budarz, J.F.; Wiesner, M. Impact of aggregate size and structure on the photocatalytic properties of TiO_2 and ZnO nanoparticles. *Environ. Sci. Technol.* **2012**, *46*, 6934–6941. [CrossRef]
36. Aldeen, T.S.; Mohamed, H.E.A.; Maaza, M. ZnO nanoparticles prepared via a green synthesis approach: Physical properties, photocatalytic and antibacterial activity. *J. Phys. Chem. Solids* **2022**, *160*, 110313. [CrossRef]
37. Sedefoglu, N. Green synthesis of ZnO nanoparticles by Myrtus communis plant extract with investigation of effect of precursor, calcination temperature and study of photocatalytic performance. *Ceram. Int.* **2024**, *50*, 9884–9895. [CrossRef]
38. Ayyanusamy, P.; Alphonse, R.; Minakshi, M.; Sivasubramanian, R. Synthesis of Amorphous Nickel-Cobalt Hydroxides for Ni^{-} Zn Batteries. *Chem.–A Eur. J.* **2024**, *30*, e202402325. [CrossRef] [PubMed]
39. Álvarez-Chimal, R.; García-Pérez, V.I.; Álvarez-Pérez, M.A.; Arenas-Alatorre, J.Á. Green synthesis of ZnO nanoparticles using a *Dysphania ambrosioides* extract. Structural characterization and antibacterial properties. *Mater. Sci. Eng. C* **2021**, *118*, 111540. [CrossRef]
40. Tsegaye, G.; Kiflie, Z.; Mekonnen, T.H.; Jida, M. Synthesis and characterization of coffee husk extract (CHE)-capped ZnO nanoparticles and their antimicrobial activity. *Biomass Convers. Biorefinery* **2023**, *14*, 30577–30589. [CrossRef]
41. Kiwaan, H.A.; Atwee, T.M.; Azab, E.A.; El-Bindary, A.A. Efficient photocatalytic degradation of Acid Red 57 using synthesized ZnO nanowires. *J. Chin. Chem. Soc.* **2018**, *66*, 89–98. [CrossRef]
42. Ekennia, A.; Uduagwu, D.; Olowu, O.; Nwanji, O.; Oje, O.; Daniel, B.; Mgbii, S.; Emma-Uba, C. Biosynthesis of zinc oxide nanoparticles using leaf extracts of *Alchornea laxiflora* and its tyrosinase inhibition and catalytic studies. *Micron* **2021**, *141*, 102964. [CrossRef]
43. Isa, E.D.M.; Shameli, K.; Ch'NG, H.J.; Jusoh, N.W.C.; Hazan, R. Photocatalytic degradation of selected pharmaceuticals using green fabricated zinc oxide nanoparticles. *Adv. Powder Technol.* **2021**, *32*, 2398–2409. [CrossRef]
44. El Golli, A.; Fendrich, M.; Bazzanella, N.; Dridi, C.; Miotello, A.; Orlandi, M. Wastewater remediation with ZnO photocatalysts: Green synthesis and solar concentration as an economically and environmentally viable route to application. *J. Environ. Manag.* **2021**, *286*, 112226. [CrossRef]
45. Ekennia, A.C.; Uduagwu, D.N.; Nwaji, N.N.; Oje, O.O.; Emma-Uba, C.O.; Mgbii, S.I.; Olowo, O.J.; Nwanji, O.L. Green synthesis of biogenic zinc oxide nanoflower as dual agent for photodegradation of an organic dye and tyrosinase inhibitor. *J. Inorg. Organomet. Polym. Mater.* **2020**, *31*, 886–897. [CrossRef]
46. Li, J.; Li, Y.; Wu, H.; Naraginti, S.; Wu, Y. Facile synthesis of ZnO nanoparticles by Actinidia deliciosa fruit peel extract: Bactericidal, anticancer and detoxification properties. *Environ. Res.* **2021**, *200*, 111433. [CrossRef]
47. Soto-Robles, C.A.; Nava, O.; Cornejo, L.; Lugo-Medina, E.; Vilchis-Nestor, A.; Castro-Beltrán, A.; Luque, P.A. Biosynthesis, characterization and photocatalytic activity of ZnO nanoparticles using extracts of *Justicia spicigera* for the degradation of methylene blue. *J. Mol. Struct.* **2021**, *1225*, 129101. [CrossRef]
48. Mousa, S.A.; Wissa, D.A.; Hassan, H.H.; Ebnalwaled, A.A.; Khairy, S.A. Enhanced photocatalytic activity of green synthesized zinc oxide nanoparticles using low-cost plant extracts. *Sci. Rep.* **2024**, *14*, 16713. [CrossRef] [PubMed]
49. Mancuso, A.; Mottola, S.; Sacco, O.; Vaiano, V.; De Marco, I. Photocatalytic degradation of ceftriaxone using TiO_2 coupled with ZnO micronized by supercritical antisolvent route. *Nanomaterials* **2023**, *13*, 3130. [CrossRef]
50. Alamzeb, M.; Faryad, S.; Ullah, I.; Hussain, J.; Setzer, W.N. Photocatalytic Degradation of Brilliant Blue Dye Under Solar Light Irradiation: An Insight Into Mechanistic, Kinetics, Mineralization and Scavenging Studies. *J. Fluoresc.* **2025**, *35*, 9093–9111. [CrossRef] [PubMed]
51. Mandal, A.K.; Katuwal, S.; Tettey, F.; Gupta, A.; Bhattarai, S.; Jaisi, S.; Bhandari, D.P.; Shah, A.K.; Bhattarai, N.; Parajuli, N. Current research on zinc oxide nanoparticles: Synthesis, characterization, and biomedical applications. *Nanomaterials* **2022**, *12*, 3066. [CrossRef]
52. Singh, T.A.; Sharma, A.; Tejwan, N.; Ghosh, N.; Das, J.; Sil, P.C. A state of the art review on the synthesis, antibacterial, antioxidant, antidiabetic and tissue regeneration activities of zinc oxide nanoparticles. *Adv. Colloid Interface Sci.* **2021**, *295*, 102495. [CrossRef]
53. Mendes, C.R.; Dilarri, G.; Forsan, C.F.; Sapata, V.d.M.R.; Lopes, P.R.M.; de Moraes, P.B.; Montagnolli, R.N.; Ferreira, H.; Bidoia, E.D. Antibacterial action and target mechanisms of zinc oxide nanoparticles against bacterial pathogens. *Sci. Rep.* **2022**, *12*, 2658. [CrossRef] [PubMed]
54. Hwang, C.; Choi, M.H.; Kim, H.E.; Jeong, S.H.; Park, J.U. Reactive oxygen species-generating hydrogel platform for enhanced antibacterial therapy. *NPG Asia Mater.* **2022**, *14*, 72. [CrossRef]

55. Weng, B.; Zhang, M.; Lin, Y.; Yang, J.; Lv, J.; Han, N.; Xie, J.; Jia, H.; Su, B.-L.; Roeffaers, M.; et al. Photo-assisted technologies for environmental remediation. *Nat. Rev. Clean Technol.* **2025**, *1*, 201–215. [CrossRef]
56. Cao, J.; Liu, H.; Qi, Z.; Liu, J.; Chen, G.; Wu, D.; Wu, Y.; James, T.D.; Li, G. The resistance of *Salmonella enterica* serovar Typhimurium to zinc oxide nanoparticles. *Nano Today* **2025**, *62*, 102687. [CrossRef]